

Luca Lobuono¹, David MacManus¹, Robert Christie¹, Luca Boscagli¹

¹ Centre for Propulsion and Thermal Power Engineering, School of Aerospace, Transport and Manufacturing, Cranfield University, Bedfordshire, MK43 0AL, UK

Abstract

The design of aero-engine intakes for compact nacelles can be an important contributor in achieving cruise fuel burn reductions. A key aspect for the design of viable compact intakes is considerations of the off-design crosswind and high incidence conditions. The aerodynamics of compact intakes is also notably dependent on the flow interaction with the fan. This work analyses the unsteady intake-fan interactions under crosswind conditions. The effect of crosswind velocity is evaluated together with the intake ground plane interaction and the unsteady aerodynamic coupling between the intake and fan. The overall aim of the research is to identify the flow structures and the unsteady mechanisms involved in the separation of the intake flow. The work uses an unsteady fully coupled time resolved Reynolds averaged Navier-Stokes computational method to identify the unsteady features of intake-fan flow separation in crosswind operations. The unsteady intake flow distortion is assessed as well as the spectral signatures and engine-order perturbations due to the unsteady flow distortion. Local separated regions were identified in the diffuser. These are associated with the characteristics of the boundary layer and are phase-locked with the local pressure pulses from the fan. This aspect should be considered in the design of compact intakes with relatively high diffusion. Additional assessments of the previously reported unsteady lip separation is provided with the identification of the frequencies of the flow features in post-separation conditions and the axial and azimuthal movement of the separation due to the interaction with the ground vortex.

Keywords: Aerodynamics, crosswind, ground effect, intake, fan

1. General Introduction

Reductions in aircraft emissions will rely on system efficiency improvements with advances in propulsion and airframe design [1]. A reduction in specific thrust, typically with an associated increase in fan diameter, will provide a benefit in propulsive efficiency and, consequently, emissions and noise [2], [3]. However, larger nacelle diameters usually also imply a potential detrimental effect from additional mass and drag [4]. Moreover, a closer proximity of the engine to the ground could cause a more adverse aerodynamic interaction between the engine and the ground plane [5]. Within this context, the design of viable aero-engine intakes is a key aspect in achieving cruise fuel burn reductions. Compact intakes are potentially able to provide cruise drag benefits as well as a reduction in the mass of the overall propulsion system [3]. High incidence and crosswind conditions are particularly critical in the design of such intakes [6]. The subsonic adverse pressure gradients in the diffuser or the lip shock are typically responsible for boundary layer separation. However, the unsteady effects of ground vortex (GV), upstream travelling perturbations from the fan and intake flow unsteadiness are not fully understood. Moreover, steady Reynolds Averaged Navier Stokes (RANS) and conventional distortion descriptors do not account for the unsteady flow features and are likely to be inadequate for novel intake design requirements.

.

1.1 Intake flow separation & distortion

An intake operating at constant crosswind speed with a variable mass flow typically encounters three different flow regimes [7]. At low mass flow conditions, the adverse pressure gradients in the diffuser part of the intake are responsible for a large separation on the windward side. The flow can reattach at higher flow regimes; however, a further increase in mass flow generates a shock over the lip, which can interact with the boundary layer on the intake surface and cause flow separation. Shock induced separation can also arise at greater crosswind speeds [8]. The separated regions are characterised by total pressure losses and extensive flow distortion which can have the potential to act as initiators of fan stall [9], [10], [11]

Another source of flow distortion is due to the ground vortex which forms under crosswind operating conditions. This flow feature is generated by the interaction between the captured stream tube and the ground plane, and it is responsible for a total pressure loss and swirl distortion at the Aerodynamic Interface Plane (AIP) [5], [12]. Additional 'trailing vortices' can arise on the leeward side of the intake but are within the captured stream tube and ingested by the engine [13], [14]. This also can give rise to total pressure and swirl distortion within the intake. For example, for an intake operating at high crosswind speed there is a supersonic region on the windward lip with a shock-boundary layer interaction (SBLI) close to the bottom dead centre which results in a separation as denoted by the iso-surface of zero axial velocity (V_{ax} =0) (Figure 1). Other small separated regions arise in the diffuser on the windward side of the intake. The interaction of the captured stream tube with the ground plane generates a ground vortex. On the windward side two trailing vortices are observed.

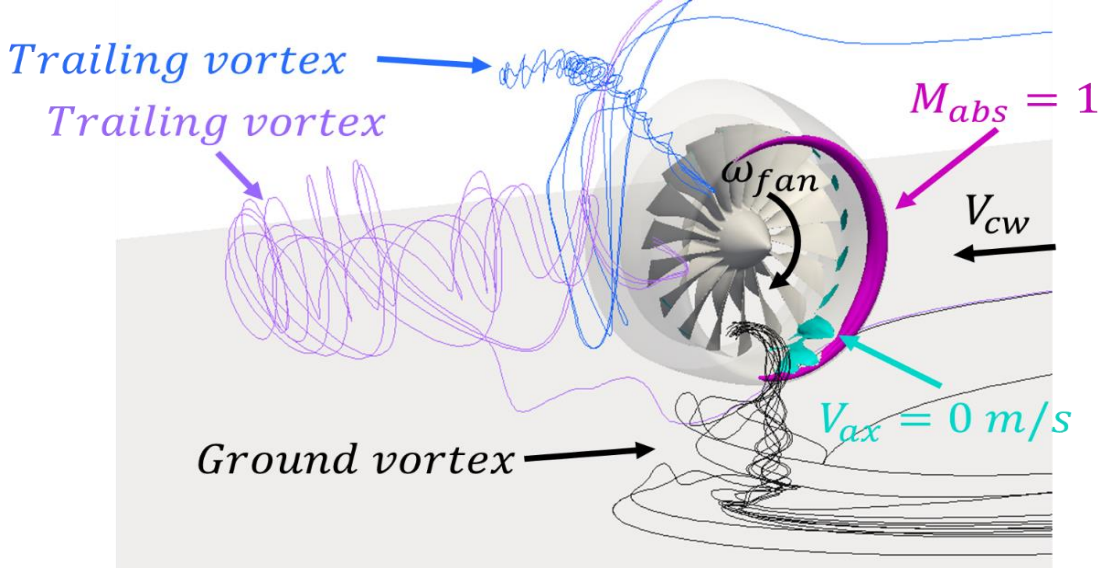


Figure 1 – Flow features of an intake in crosswind.

1.2 Intake-fan aerodynamic interactions

Several flow features within the intake interact. The shock or the intake diffusion are responsible for separated boundary layers, but the unsteady contributions of the ground vortex and fan are not fully understood. In addition, for a relatively short intake, the fan and the intake aerodynamics are likely to be more coupled. There is limited research in the literature regarding this unsteady interaction. Several experimental [15], [16] and computational [17], [18], [19], [20] studies have examined the positive steady effect of the fan in the diffuser part of the intake under high incidence. Cao et al. [6] demonstrated that an intake-fan configuration under high incidence conditions can direct more flow towards the tip compared to an intake-only configuration. A steady RANS approach with a fan body force model was used to assess the effect of the axial location of the fan. The massflow redistribution and the flow acceleration at the tip of the fan results in a static pressure reduction that alleviates the adverse pressure gradient upstream of the fan. It was concluded that

the acceleration depends on the axial location of the fan, and the benefit was greater for the shortest intake $(L_{in}/D = 0.17)$. Boscagli et al. [21], [22] also observed a positive effect of the fan on the shock driven separation margin under crosswind. Compared to the aspirated configuration (intakeonly), the steady RANS approach with the Immersed Boundary Method for Smeared Geometry (RANS-IBMSG) fan model predicted an increase in the separation-free margin from approximately $V_{cw} = 20$ kts of the aspirated case to $V_{cw} = 28$ kts due to the steady effect of the fan. It was observed that the fan reduces the total pressure loss at the AIP and contributes to a fuller and higher momentum boundary layer due to the radial mass flow redistribution. However, Boscagli et al. [21], [22] also demonstrated a detrimental unsteady effect of the fan using the Unsteady RANS Time Resolved Fan (URANS-TRF) method. The fan generates unsteady static pressure waves which propagate upstream up to the shock front on the intake lip and decreased the threshold crosswind speed from V_{cw} = 28 kts to 24 kts. Overall, previous research has demonstrated the need for an unsteady time resolved approach to account for the interactions between the intake and fan. However, studies regarding the impact of these interactions and both numerical and experimental data are limited. Furthermore, as conventional metrics are not capable of fully describing the unsteadiness of intake distorted flows, new methods need to be explored. Therefore, the scope of this work is to address the unsteady aerodynamic interaction between intake and fan and to evaluate and quantify the post-separation distortion and the related flow characteristics. The novelty of the work consists in the analysis of unsteady data from attached to grossly separated conditions of a compact intake coupled with a fan with an increase in crosswind velocity.

2. Methodology

2.1 Intake design, meshing and computational grid

This paper explores the unsteady aerodynamic interactions between a full-scale low-speed fan and a compact intake for a range of crosswind speeds. The intake is a research geometry designed using the in-house Tool for Intake Design (TIDE) method [23]. This uses a parametric approach based on iCST curves to generate 2D and full 3D axisymmetric and non-axisymmetric geometries. The geometry is a full-scale compact intake with $L_{in}/D_{fan}=0.4$ and a ground clearance of $H/D_{hi}=0.44$, where H is the distance of the bottom lip from the ground and D_{hi} is the highlight diameter. A full 3D structured mesh of $4\cdot10^7$ cells was generated with ICEM [24]. The wall boundary layer was resolved with a $y^+=1$. The overall computational domain (Figure 2) is approximately a quarter of a sphere with radius ~30 times the fan diameter (based on [25]). At the freestream, static pressure far-field boundary conditions are applied. The intake, fan cowl, spinner, and ground plane are modelled as no-slip walls.

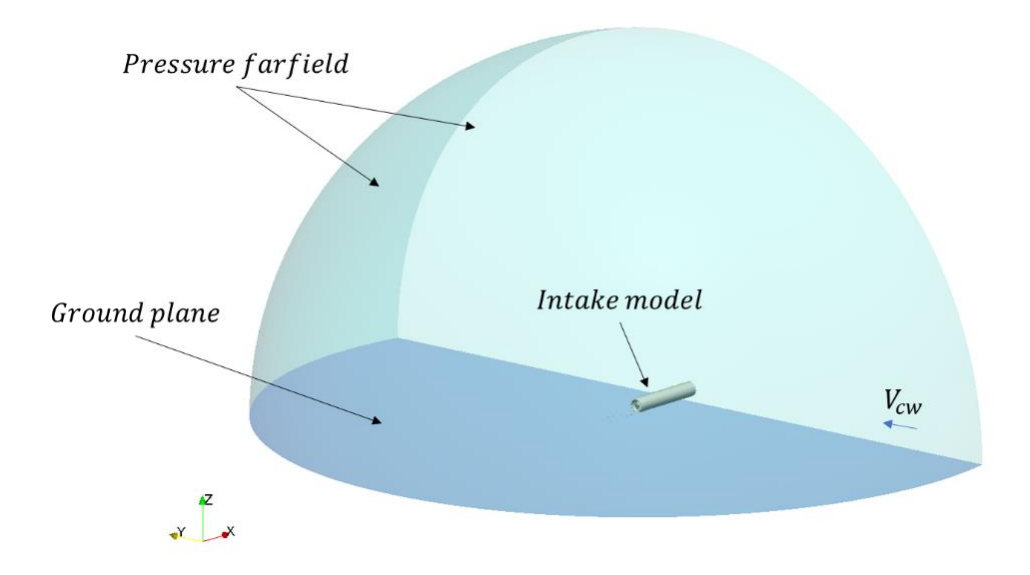


Figure 2 - Computational domain.

2.2 Solver & coupled intake-fan CFD analysis

The computations are performed with HYDRA which is an unstructured finite volume solver [26] [27]. An explicit solver is used for the time resolved computations. The aerodynamic interaction between the intake and the fan is assessed with an unsteady fully coupled intake-fan CFD method. It is based on the methodology adopted by Boscagli et al. [21], [22], [28]. The method is an unsteady Reynolds Averaged Navier Stokes approach with full annulus rotating fan (URANS-Time Resolved Fan or URANS-TRF). The configuration comprises the intake coupled with a research bypass and core fan stage with a single passage Outlet Guide Vane (OGV) and single passage Engine Sector Stator (ESS) blades (Figure 3). A sliding plane boundary condition is applied at the full annulus fanintake interface. A mixing-plane boundary condition is used at the interface between fan-OGV and fan-ESS domains. A constant mass flow is prescribed at the OGV and ESS outlets.

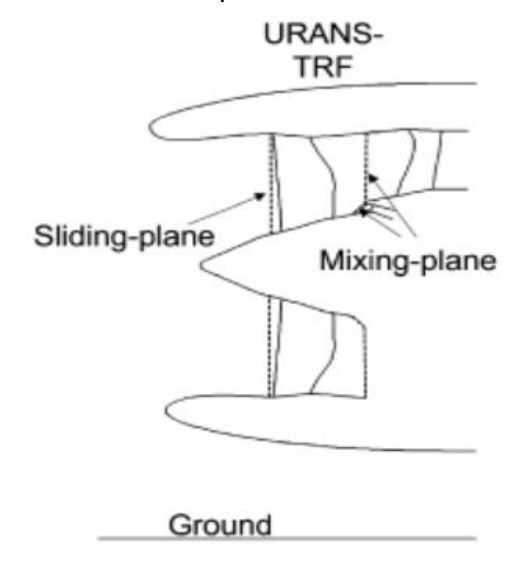


Figure 3 - Fully coupled intake-fan configuration with sliding plane condition at the intake-fan boundary and mixing plane at the fan-OGV and fan-ESS boundaries [22].

The Spalart-Allmaras (SA) turbulence closure model is used based on previous computational studies of intakes operating at off-design conditions with body-force fan models [6], [18], [29]. The URANS-TRF uses a timestep correspondent to 60 times the blade passing frequency f_{bp} and a total simulation time of 6 fan revolutions after an initial transient. The data is sampled every 12 timesteps (sampling frequency of $f_s/f_{bp}=5$). A total of $N_s=540$ samples is collected; this means a frequency resolution of $f_{res}/f_{bp}=(f_s/f_{bp})/N_s\sim0.01$ is achieved.

2.3 Unsteady Post Processing

A series of methods for the post processing of unsteady intake data have been developed. These techniques include the discrete Fourier transform to decompose a time or space varying quantity in a series of waves, which can be studied to determine the frequency or engine order signatures [28]. Distribution of aerodynamic quantities are assessed at the Aerodynamic Interface Plane (AIP) and on the unwrapped intake surface. The isentropic Mach number is calculated with eq. (1), where P_0^{∞} is the freestream total pressure, P the local static pressure and γ the ratio of specific heats.

$$M_{lse} = \sqrt{\left(\left(\frac{P_0^{\infty}}{P}\right)^{\frac{\gamma-1}{\gamma}} - 1\right) \cdot \frac{2}{\gamma - 1}} \tag{1}$$

Conventional total pressure distortion descriptors are also evaluated. These are DC60 (eq.(2))[30], overall Circumferential Distortion Index (IDC - eq.(3)) [31], overall Radial Distortion Index (IDR - eq. (4)) [31], ring Circumferential Distortion Index (IDC_h - eq.(5) [31], ring Radial Distortion Index (IDR_h - eq.(6)) [31].

$$DC60 = \frac{\bar{P}_{0,60} - \bar{P}_{0,AIP}}{\bar{q}_{AIP}} \tag{2}$$

$$IDC = \max\left[\frac{1}{2}(IDC_h + IDC_{h+1})\right]$$
(3)

$$IDR = \max[IDR_1, IDR_N] \tag{4}$$

In eq. (2) $\bar{P}_{0,60}$ is the lowest area-averaged total pressure in a 60° sector at the AIP, $\bar{P}_{0,AIP}$ the area-averaged total pressure at the AIP and \bar{q}_{AIP} is the area averaged dynamic head calculated from the interpolation on a $12\times30^\circ$ rake. In eq.(3), h is the ring index and IDC_h and IDC_{h+1} are the h-th and (h+1)-th ring circumferential distortion indices calculated with eq.(5). $\bar{P}_{0,h}$ and $P_{0\,min,h}$ are the average and minimum value of total pressure of the h-th ring. In eq. (4) IDR_1 and IDR_N are the ring radial distortion indexes (IDR_h), which are calculated with eq.(6).

$$IDC_{h} = \frac{\bar{P}_{0,h} - P_{0 \, min,h}}{\bar{P}_{0,AIP}} \tag{5}$$

$$IDR_{h} = \frac{\bar{P}_{0,AIP} - \bar{P}_{0,h}}{\bar{P}_{0,AIP}} \tag{6}$$

The time variation of DC60 is analysed, and the signals are evaluated using a discrete Fourier transform method implemented in a Fast Fourier Transform (FFT) algorithm [32]. This allows to identify the dominant frequencies of the time variant signals. A temporal FFT is used also to determine the banded spectra of total pressure at the Aerodynamic Interface Plane (AIP) and static pressure on the intake surface. Equi-spaced frequency intervals of 6 $f_{res}/f_{bp} \sim 0.06$ are chosen for the spectral bands.

Recent studies have demonstrated that swirl distortion should be considered an important aspect of intake flow distortion [33], [34]. The swirl angle and relative swirl angle are defined with eq. (7) and (8), where V_{θ} , V_{ax} and U represent the tangential absolute, axial, and blade velocities, respectively.

$$\alpha = \tan^{-1} \left(\frac{V_{\theta}}{V_{ax}} \right) \tag{7}$$

$$\beta = \tan^{-1} \left(\frac{U - V_{\theta}}{V_{ax}} \right) \tag{8}$$

In this work, the swirl intensity (SI) is chosen to quantify the distortion at different radial locations. SI is a SAE distortion descriptor defined on a ring-by-ring basis (Eq.(9)) [35]. In eq.(9), (10), and(11), h is the ring index; k is a strictly positive or strictly negative swirl region in the h-th ring. Positive and negative Sector Swirls (SS^+ , SS^-) are defined for each k-th region in the h-th ring as the average swirl angle obtained integrating over the $\theta_{h,k}^{\pm}$ arc (Eq.(10),(11)).

$$SI_{h} = \frac{\sum_{k=1}^{m} SS_{h,k}^{+} \theta_{h,k}^{+} + \sum_{k=1}^{m} \left| SS_{h,k}^{-} \right| \theta_{h,k}^{-}}{360}$$
(9)

$$SS_{h,k}^{+} = \frac{1}{\theta_{h,k}^{+}} \int_{\theta_{h,k}^{+}} \alpha(\theta)_h d\theta \tag{10}$$

$$SS_{h,k}^{-} = \frac{1}{\theta_{h,k}^{-}} \int_{\theta_{h,k}^{-}} \alpha(\theta)_h d\theta \tag{11}$$

The FFT is used to decompose the time signal of the distortion metrics and to identify the banded spectra of aerodynamic quantities such as total and static pressure.

$$i = \beta - \beta_m \tag{12}$$

The spatial harmonics (Engine orders-EO) of blade incidence (eq.(12)), where β_m is the blade metal angle) are identified with a circumferential FFT decomposition (eq. (13)) [21].

$$\widehat{\iota'}(t, k_{n_{\theta}}) = \sum_{n_{\theta}=0}^{2\pi} \widehat{\iota'}(t, k_{n_{\theta}}) e^{\frac{2\pi j k_{n_{\theta}}}{N_{\theta}}}, where \ 0 \le k \le N_{\theta}$$
(13)

j is the imaginary unit, $k_{n_{\theta}}$ is the discrete wavenumber, N_{θ} is the number of samples in the circumferential direction, i' is the instantaneous azimuthal distribution of blade incidence at fixed radius, and $\widehat{\iota'}$ is the array with the spatial Fourier coefficients (amplitude, phase). The engine-order is the normalised discrete wavenumber $EO=k_{n_{\theta}}/2\pi$.

3. Results

The results section is divided into two main parts. Section 3.1 focuses on the analysis of the intake separation characteristics, while section 0 analyses the features of post-separation distortion. In both sections the effect of a varying crosswind speed is assessed (20, 22, 26 and 30 kts) at fixed intake mass flow and ground clearance. The configuration is such that the crosswind direction (at ϕ =90°Figure 4) results in a counterclockwise rotating ground vortex. Consequently, the fan and the GV are counter-rotating.

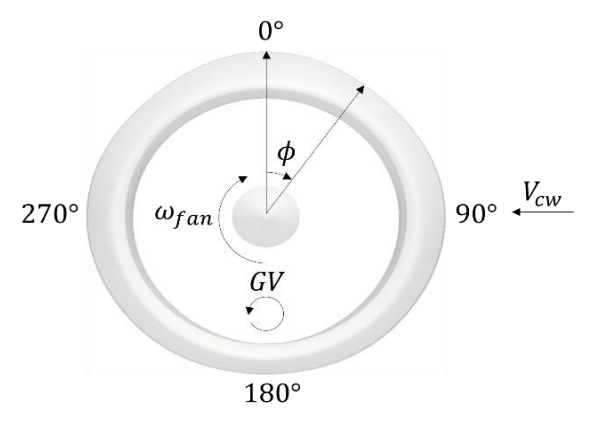


Figure 4 - Crosswind configuration with counter-rotating ground vortex

3.1 Separation characteristics

At all the considered crosswind speed (20, 22, 26, 30 kts) there is a shock on the windward side of the intake (contour line of $M_{ise}=1$ in Figure 5 (a-d)). The shock interacts with the boundary layer and results in a local separation for the cases at 20, 22, and 26 kts crosswind. This characteristic was previously also reported by Boscagli [22]. For example, this is evident in the indicated contour line of axial wall shear stress $T_{wx}=0$ in the lower region around $\phi=180^\circ$. At 20kts crosswind, after an initial transient phase, this is a local closed separation (Figure 5 (a)). At greater crosswind speeds the separation grows and extends both axially, towards the AIP, and tangentially in the counterclockwise direction (counter-rotating compared to ω_{fan}) (Figure 5 (b), (c)). While the growth of the separation is associated with a stronger shock, the tangential translation of the separation may be related to the ground vortex which induces tangential momentum in the counterclockwise direction. For brevity, this separation characteristic is referred to as A.

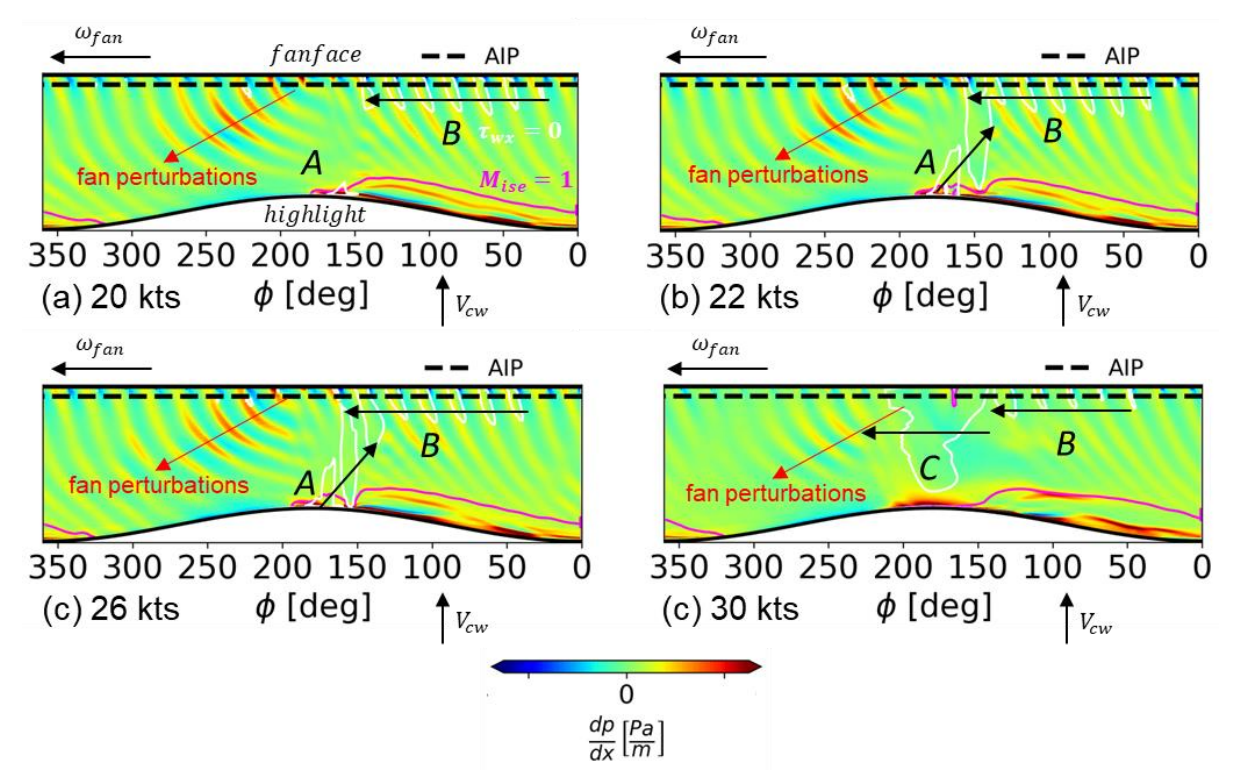


Figure 5 – Time snapshots of dp/dx on the unwrapped intake surface with contour lines of $M_{ise}=1$ and $T_{wx}=0$ at (a) 20, (b) 22, (c) 26, and (d) 30 kts.

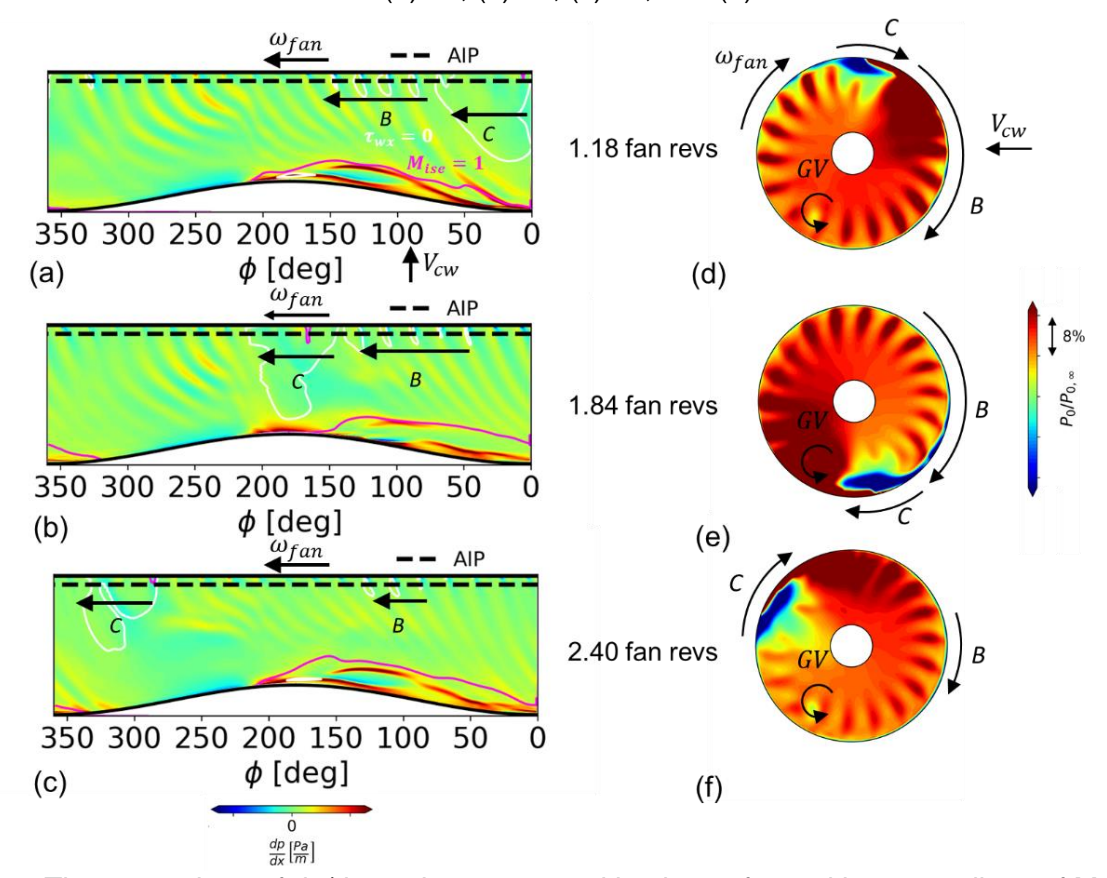


Figure 6 - Time snapshots of dp/dx on the unwrapped intake surface with contour lines of $M_{ise}=1$ and $\tau_{wx}=0$ at 30 kts at (a) 1.18, (b) 1.84, (c) 2.40 fan revolutions; Time snapshots of $P_0/P_{0,\infty}$ at the AIP at 30 kts at (a) 1.18, (b) 1.84, (c) 2.40 fan revolution

Other separated regions (T_{wx} =0 in Figure 5 (a-d)) arise in the diffuser part of the intake on the windward side (25°< ϕ <150°) and just ahead of the fan blades. In this work these are referred to as characteristic *B*. These are associated with the nature of the boundary layer in the diffuser and are phase-locked with the local effects of the upstream pressure signatures from the fan. The small

regions of separation rotate with the fan in a clockwise direction. Depending on the crosswind velocity, the two different separation characteristics (A, B) interact. For example, for a crosswind velocity of 20 kts, the interaction between the two flow separations is limited because A does not extend towards the AIP after the initial transient phase. Then, at 22 and 26 kts the lip separation extends downstream and merges with the local diffuser separations. For a further increase in V_{cw} to 30 kts, the separation grows until there is a gross unsteady separation which rotates at about 70% of the fan rotational speed (Figure 6).

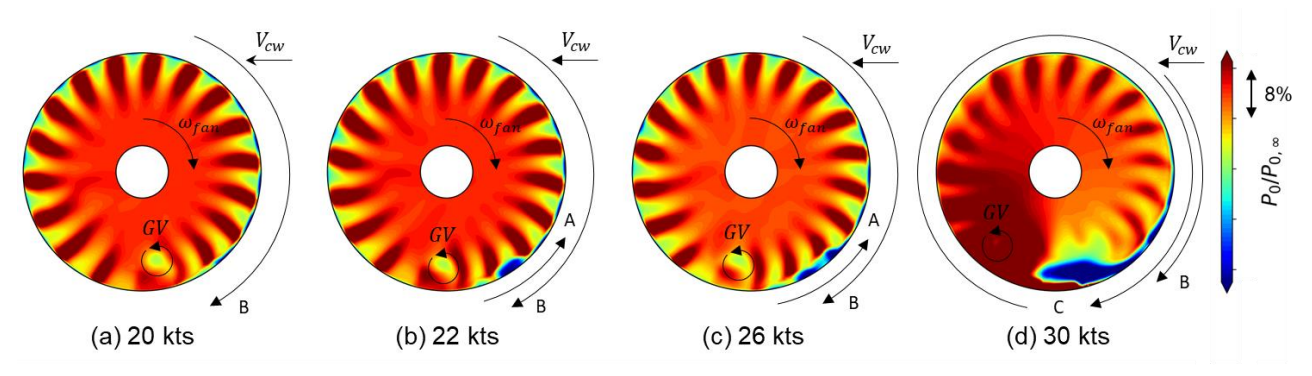


Figure 7 – Time snapshots of $P_0/P_{0,\infty}$ at the AIP at (a) 20, (b) 22, (c) 26, and (d) 30 kts.

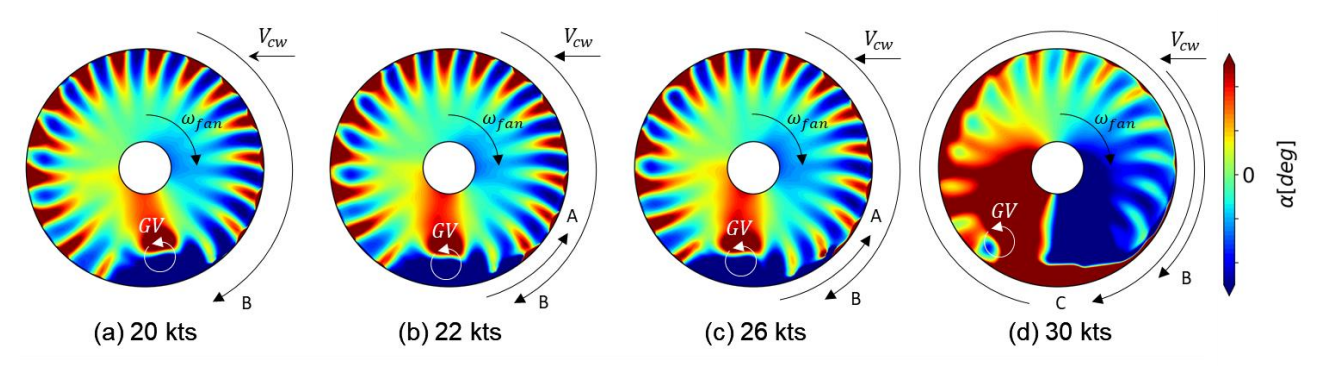


Figure 8 – Time snapshots of swirl angle α at the AIP at (a) 20, (b) 22, (c) 26, and (d) 30 kts.

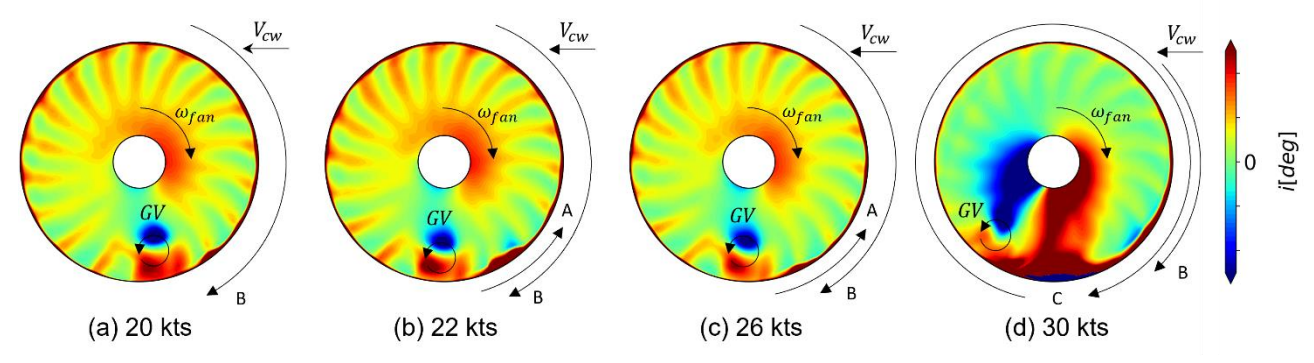


Figure 9 - Time snapshots of blade incidence i at (a) 20, (b) 22, (c) 26, and (d) 30 kts.

Along with the GV, these separations result in total pressure deficits at the AIP (Figure 7(a-c)). These are also evident in Figure 1, which is a snapshot of the unsteady flow field at V_{cw} =26kts.The ground vortex generates local negative swirl at the fan tip and positive swirl close to the hub (Figure 8). The local negative swirl is responsible for an increase in blade incidence (Figure 9). This results in stronger fan shocks and perturbations that originate at the fan-face at ϕ =180° and rotate in a clockwise direction on the leeward side of the intake (Figure 5 (a-d)). Boscagli et al [21] also observed that the amplitude of fan tip pulsation can increase as the fan crosses the ground vortex. When the pressure pulses reached the shock front, the amplitude of the fluctuations of the axial displacement of the shock location was increased. However, compared with the results reported in [21] the distribution of dp/dx in Figure 5 (a-c) do not show the same evident interaction between the fan pressure pulses and the shock front for this different intake design and conditions.

3.2 Post-separation distortion

This section investigates the post-separation distortion with conventional distortion descriptors and provides an insight into the flow features with temporal FFTs of total pressure and static pressure and a spatial FFT of the blade incidence angle.

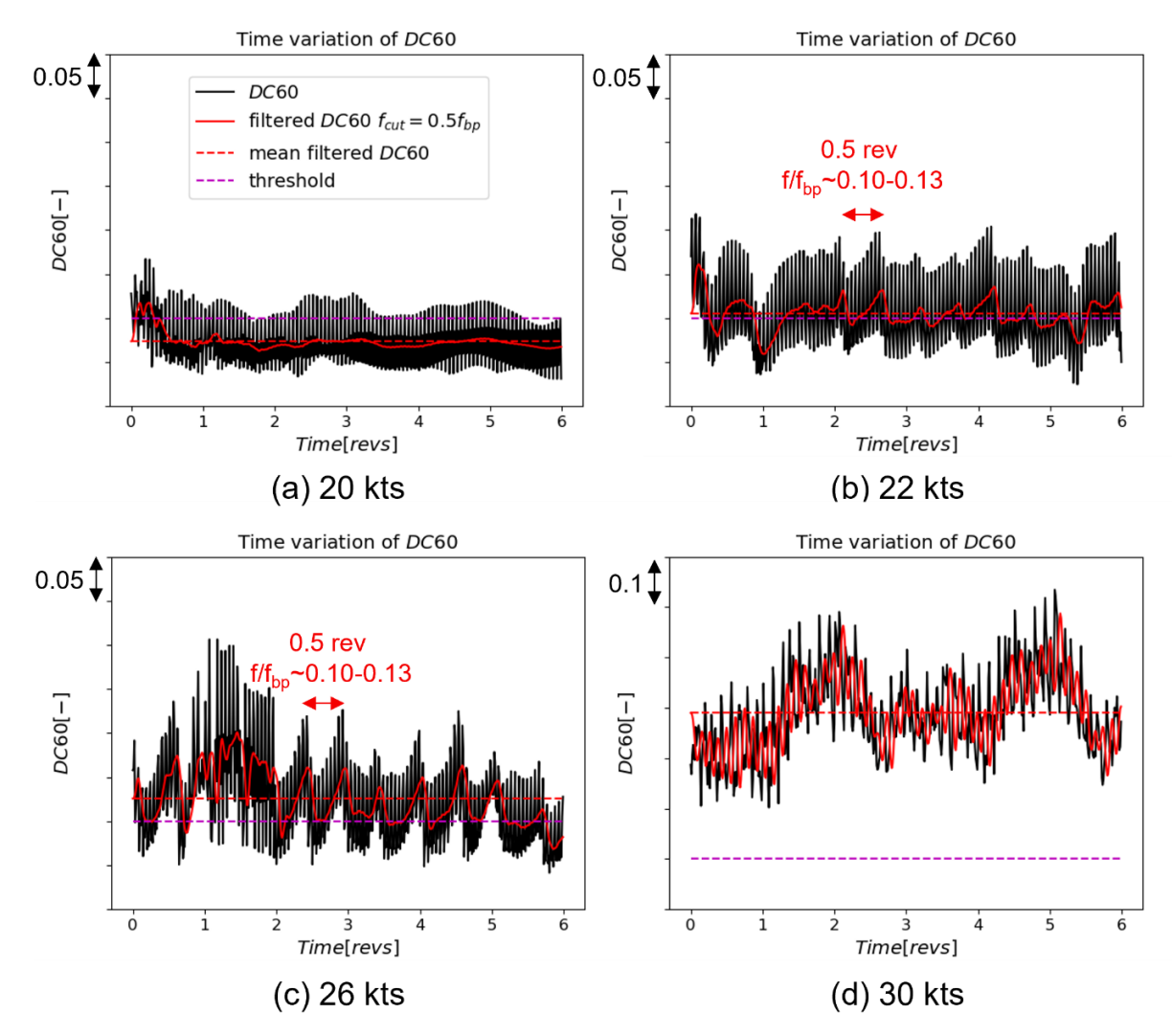


Figure 10 - DC60 and filtered DC60 time variation at 20(a), 22(b), 26(c), and 30 kts.

The time variation of DC60 (black line in Figure 10) is highly unsteady and is a combination of both high and low frequency content. Three main characteristic frequencies are evident at V_{cw}=20 kts (Figure 11 (a)), 22 and 26 (Figure 11 (b)) kts. High frequency perturbations are related to the blade passing and its first super-harmonic. The low frequency flow features are observed in the range $0.01 \le f/f_{bp} \le 0.22$. Since the high frequencies ($f/f_{bp} \ge 1$) originate from the fan itself, they are not distortion peaks for the fan. Therefore, a low-pass filter with cut-off frequency of fcut=0.5fbp is applied to the variation of DC60 to mask the effect of blade-passing related disturbance (red solid line in Figure 10). The mean value of filtered DC60 (red dashed line in Figure 10) increases from -0.03 below the threshold at 20 kts to +0.03 above the threshold at 26 kts. At 22 kts it is just above the threshold which is the condition at which the leading-edge separation (A) evolves towards the AIP. That indicates that the increase of total pressure distortion at the AIP is mainly associated with the lip separation and the development within the diffuser. At V_{cw}=22 and 26 kts, there is a temporal wavelength of the filtered DC60 of approximately 0.5 revolutions (Figure 10 (b), (c)), which corresponds to a frequency f/f_{bp} of 0.10-0.13 (Figure 11 (b), Figure 12 (b)). In comparison with the low frequency signatures at 20 kts (Figure 12 (a)), at 26kts the separation increases the low frequency amplitudes especially within the 0.01-0.02 and 0.1-0.13 ranges of f/f_{bp} (Figure 12 (b)). At 30 kts the intake flow is grossly separated, and levels of unsteady total pressure distortion are significantly above the nominal threshold (Figure 10 (d)).

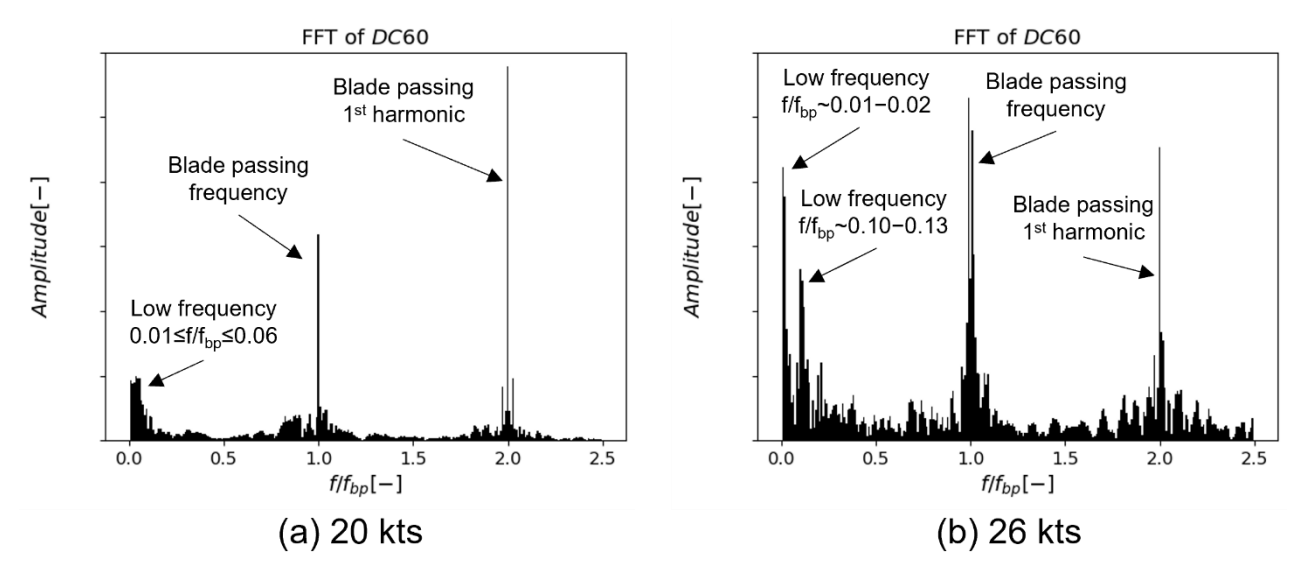


Figure 11 - FFT harmonic decomposition of DC60 time variation at 20 (a) and 26 (b) kts.

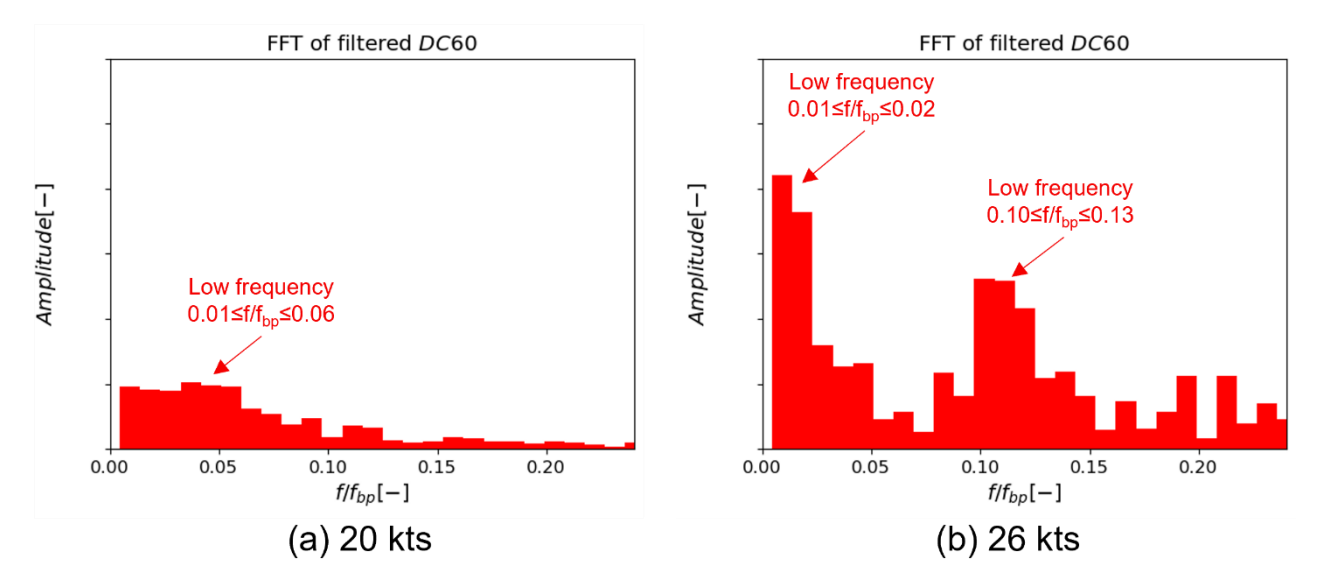


Figure 12 - FFT harmonic decomposition of filtered DC60 time variation at 20 (a) and (b) limited to frequencies f/f_{bp}≤0.24.

The banded spectra analysis with the temporal FFT decomposition of P_0 (Figure 13) at the AIP is used to identify the flow features that belong to the frequency range $0 \le f/f_{bp} \le 0.22$ for the $V_{cw} = 26$ kts case. The frequencies have been divided in four equi-spaced ranges with $f/f_{bp} = 0.06$ intervals. While the higher frequency bands are all related to the separation (Figure 13 (b-d)), the lowest frequency range (Figure 13 (a)) is associated with the separation, but also with unsteadiness associated with the Ground Vortex (GV) and Trailing Vortex (TV). This is also partially reflected in the overall spectral signature (Figure 12) which compares the attached ($V_{cw} = 20$ kts) and separated ($V_{cw} = 26$ kts) configurations. For example, at 20 kts the lip and diffuser separations have little impact on the temporal variation of total pressure, and the distortion is mainly related to the GV and TV. In contrast, at 26 kts (Figure 13) the impact of the separation is noted across for $f/f_{bp} \le 0.24$.

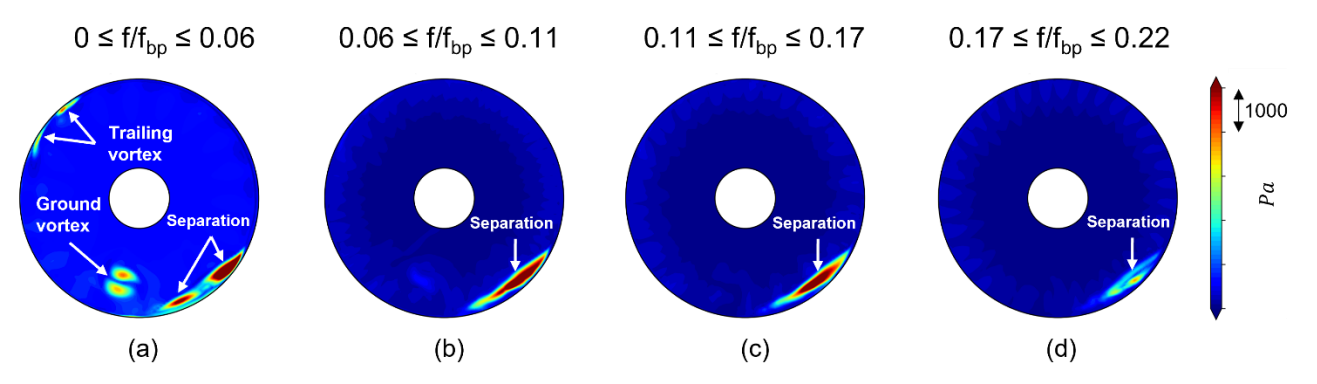


Figure 13 - Banded spectra of total pressure at the AIP with frequency ranges f/f_{bp} within (a) 0-0.06, (b) 0.06-0.11, (c) 0.11-0.17, (d) 0.17-0.22 at the AIP at 26kts.

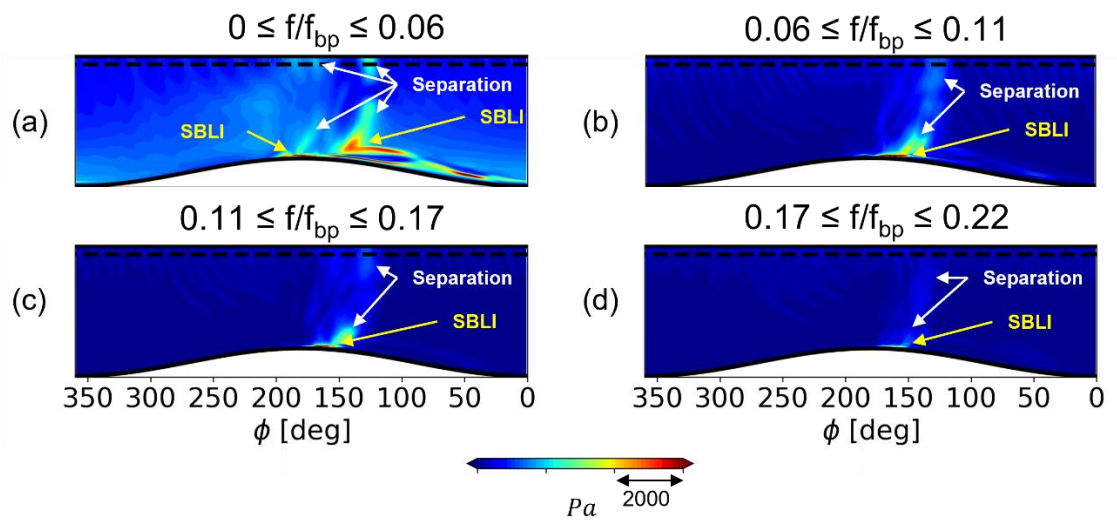


Figure 14 - Banded spectra of static pressure on the unwrapped intake surface with frequency ranges f/f_{bp} within (a) 0-0.06, (b) 0.06-0.11, (c) 0.11-0.17, (d) 0.17-0.22 at the AIP at 26kts.

The unsteady signatures of the SBLI and the main separation are also evident in all four frequency spectral bands of static pressure on the unwrapped intake surface (Figure 14). At the frequencies from $0.06 \le f/f_{bp} \le 0.22$ the lip separation and shock movement are the main features (Figure 14 (b-d)). However, there is also evidence of the separation that then extends along the diffuser and towards the fan face. In the lowest frequency band of $0 \le f/f_{bp} \le 0.06$ (Figure 14 (a)) the signature is dominated by the SBLI which extends over a large portion of the intake lip as well as the associated separation within the diffuser. In this low frequency band $(0 \le f/f_{bp} \le 0.06)$ there is a very modest indication of the unsteadiness of the ground vortex which is off the surface and more clearly noted in the AIP distributions at $0 \le f/f_{bp} \le 0.06$ (Figure 13 (a)). This partially indicates that there may be a linked unsteady interaction between the GV and the lip separation at these low frequencies. For example, at 20kts, when there is no notable lip separation, the GV unsteadiness is in the flow frequency $0.01 \le f/f_{bp} \le 0.06$ range (Figure 12 (a)). The signature of SBLI and separation on the intake surface was also reported by Boscagli [21] with similar frequencies $(0.01 \le f/f_{bp} \le 0.19)$. However, in this work for this configuration, there is a distinction between the frequency content of the ground vortex $(f/f_{bp} \le 0.06)$ from the separation and SBLI $(f/f_{bp} \le 0.22)$.

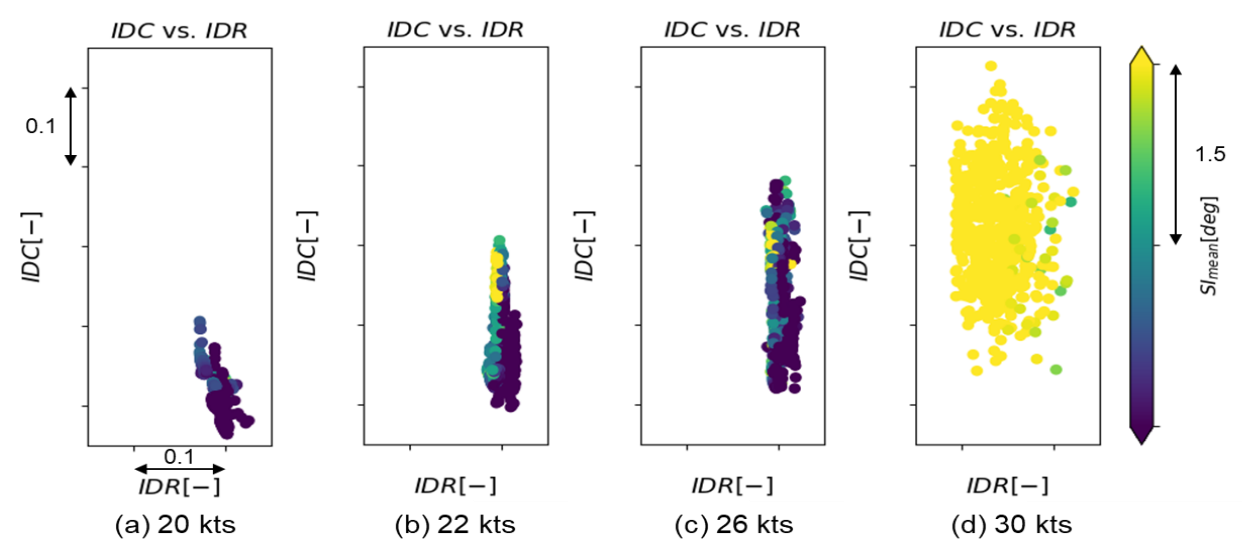


Figure 15 - IDC and IDR coloured by SI_{mean} at V_{cw} = 20(a), 22(b), 26(c) and 30(d) kts.

The circumferential and radial extents of the total pressure distortion is also reflected in the conventional circumferential (IDC) and radial (IDR) distortion metrics. For V_{cw} of 20, 22, 26 the increase in the total pressure distortion (Figure 7) is mostly limited to the circumferential extent with modest changes in the radial distortion as reflected in IDC and IDR (Figure 15). For example, the maximum values of IDC increase by 0.3 for $V_{cw} = 26$ kts compared with the 22 kts configuration. Similarly, across this range of Vcw from 20 to 26 kts, there is also an increase of about 2 degrees in the maximum values of SI_{mean} (Figure 15 (a-c)). At 30 kts, for the grossly separated case high swirl intensity is associated with both higher and lower IDC and IDR (Figure 15 (d)).

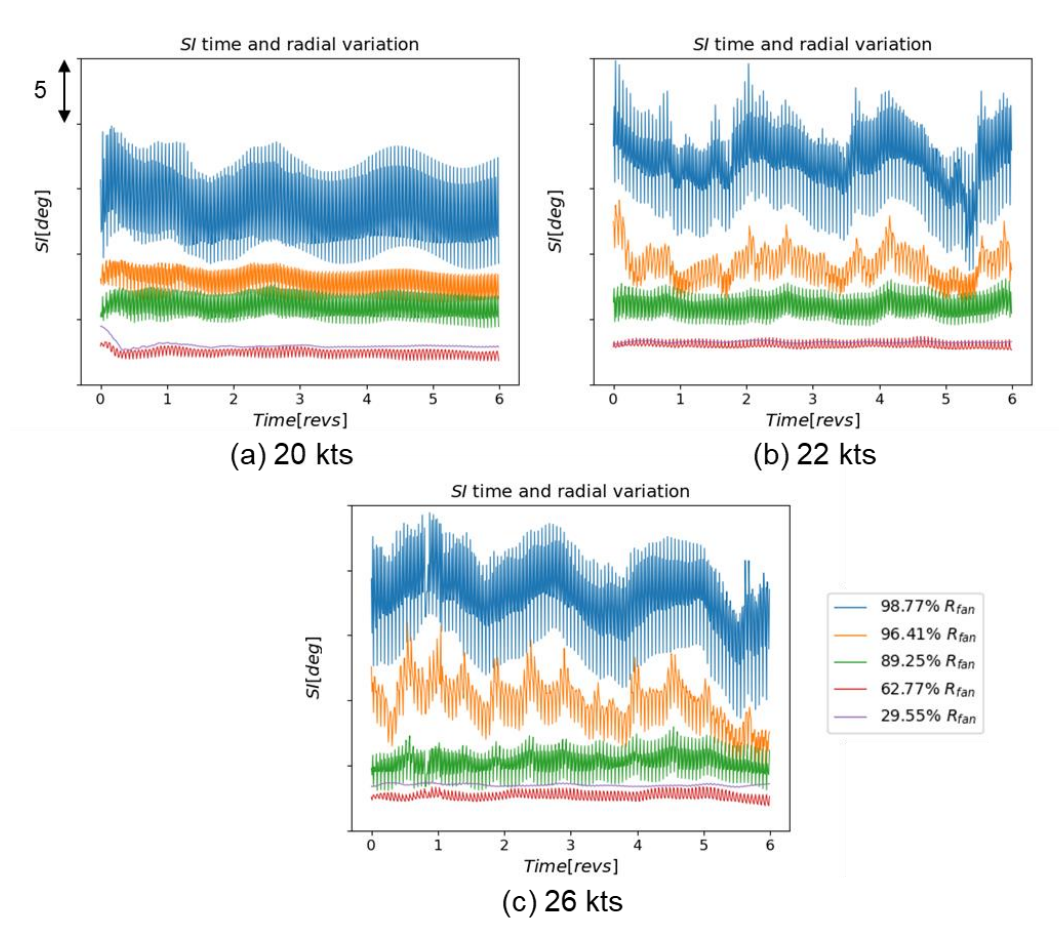


Figure 16 - Time variation of SI at different radial locations at (a) 20, (b) 22, (c) 26 kts.

The swirl distortion can also have a notable impact on the performance of a coupled intake-fan configuration. At 20 kts the time unsteady SI is characterised by mainly high frequency variations associated with the blade passing with the mean and peak values increasing with radius. At $r/R_{fan}=0.3$, the fan operates in local subsonic conditions, and there is no upstream propagation of the static pressure waves. As r/R_{fan} is increased, the fan operates in transonic regimes and the supersonic region grows with the radius. Thus, the amplitude of the static pressure pulses is also increased. The onset of separation at 22 kts (Figure 16 (b)) generates an increase in SI for $r/R_{fan} \ge 0.96$ and a medium frequency signature for $r/R_{fan} \ge 0.89$ for both the 22 and 26 kts cases (Figure 16 (b-c)). This is associated with the same 0.5 revolution temporal wavelength of DC60 at about $f/f_{bp} \sim 0.10$ -0.13 (Figure 11 (b) Figure 12 (b)). There is also evidence of the similar very low frequency oscillations which arise at the $0.01 \le f/f_{bp} \le 0.06$ range.

The incidence can impact the fan-intake aerodynamic interaction by increasing the blade loading and generating rotating pressure waves. In addition, the flow distortion can also affect the aero-mechanical response of the fan [36], [37], [38]. Thus, the impact of intake flow distortions on the engine order signatures is also important and needs to be quantified. At each radial location the circumferential variation of the blade incidence angle is decomposed into the spatial variations and considered in terms of the Engine Order (EO) where a 1-EO is a once-per-revolution distortion and an 18-EO is associated with the number of fan blades (Figure 17). The emphasis is on the frequency content and amplitudes since the objective is to identify the relationship between the flow features and the spatial variation.

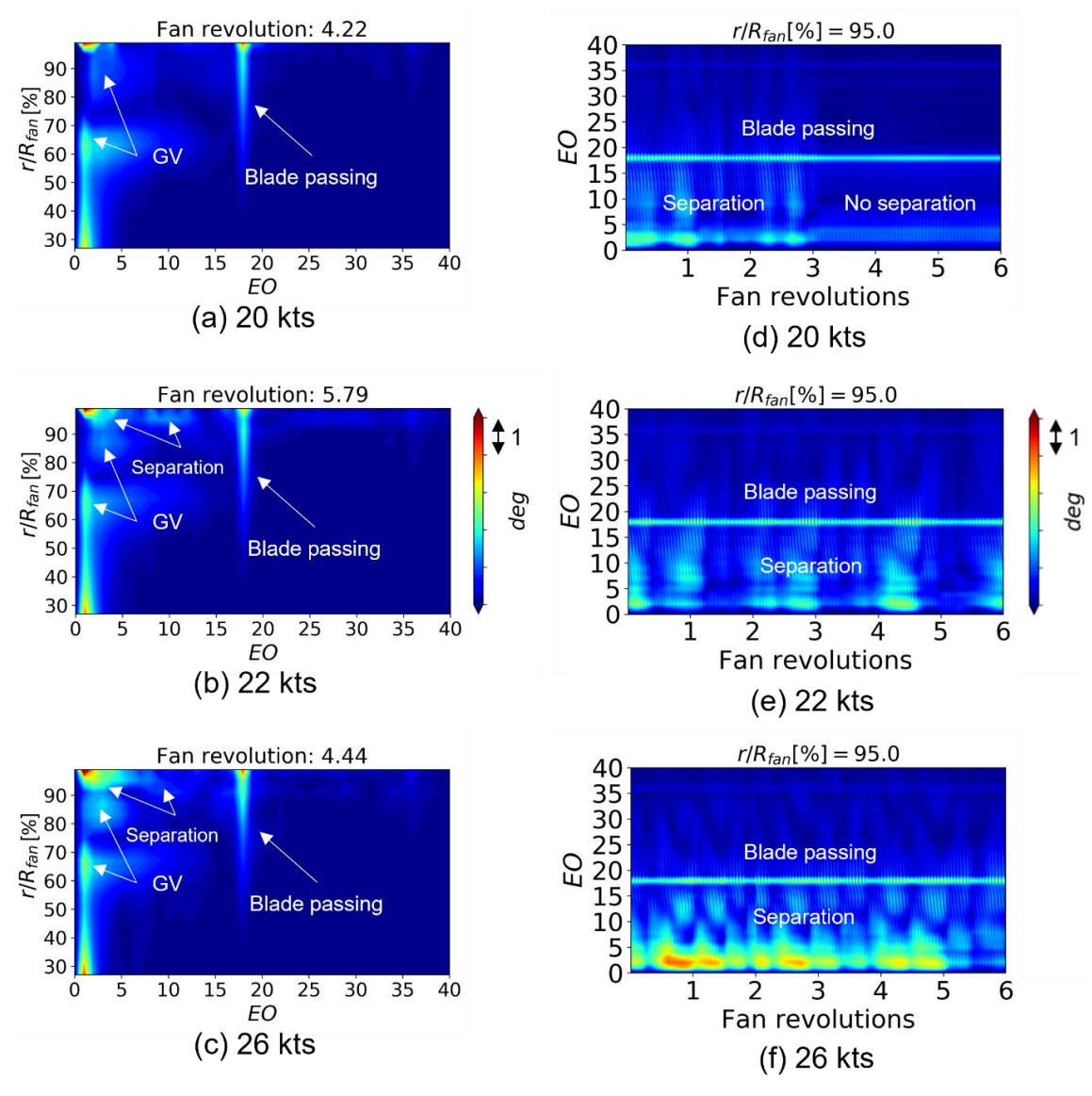


Figure 17 - Time snapshots of the amplitude of blade incidence spatial harmonics as a function of radius and frequency (EO) at (a) 20, (b) 22, (c) 26 kts. Time variation of the amplitude of blade incidence spatial harmonics at (e) 20, (f) 22, (g) 26 kts for r/R_{fan}=0.95.

Across the three crosswind speeds of 20 (Figure 17 (a)), 22 (Figure 17 (b)) and 26 (Figure 17 (c)) kts the impact of the blade passing frequencies (18 EO) on the Blade Incidence Angle (BIA) variation increases from mid-span r/R_{fan}~0.6 to the tip. Similarly to that described for SI (Figure 16), this is associated with the radial extent of the local supersonic region, which is responsible for the increase in static pressure fluctuations. Also, the GV has a clear signature with peaks of amplitude at 1-2 EO at mid-span (0.6≤r/R_{fan}≤0.7), and at the tip (r/R_{fan}≥0.95). Smaller amplitudes are also observed 3-5 EO closer to the tip (0.8≤r/R_{fan}≤0.9). The separation arising at 22kts (Figure 17 (b) (c)) causes low frequency signatures at 1-5 EO and 7-15 EO at the tip r/R_{fan}≥0.95. This effect is more evident where the EO amplitudes are plotted against time (Figure 17 (d-f)). At 22 (Figure 17 (e)) and 26 (Figure 17 (f)) kts the separation is responsible for peaks of amplitude at 1-5 EO and scattered variations in the range of 7-15 EO. The impact of the separation is evident at 20 kts (Figure 17 (d)). A transient with a separation similar to characteristic A occurs in the first three fan revolutions. Once this decays out, the last three observed revolutions are free from this flow feature (Figure 17 (d)). For 22 and 26 kts, the signatures of the flow frequency separations are also evident. For example, at 22 kts (Figure 17 (e)) there are intermittent augmentations for 1-10 EO range, while at 26 kts (Figure 17 (f)) this changes to a relative clear intermittency at about 0.5 revolution period across the 1-15 EO range. This differs from the periodic behaviour reported in [21] which increased the amplitude of the 2-EO and the 5-EO spatial harmonics every 2 fan revolutions. This may be due to the different intake geometries and operating conditions which are affecting the EO signatures associated with the intake distortion.

4. Conclusions

This research has explored the impact of the crosswind speed on the unsteady aerodynamics of a coupled intake-fan configuration. Two main aspects have been analysed, one is the intake-fan separation characteristics, and the other one is the post-separation flow distortion.

Local separated regions were identified upstream of the fan. These are associated with the modulation of the intake diffusion by the pressure pulses from the fan. An axial and tangential movement of the shock-driven separation was also observed. This is related to the interaction of the shock-driven separation with the ground vortex. Both characteristics can affect and guide the design of compact intakes. It is commonly believed that the fan can have a positive impact on the adverse pressure gradients [6], [15], [16], [17], [18], [20], [22], but this work demonstrated that the fan pressure pulses can affect the diffusing boundary layer by locally increasing and decreasing the static pressure. Therefore, this characteristic should be considered in the design of highly diffusive intakes. Furthermore, there is the potential to improve the interaction between the shock, the boundary layer, and the ground vortex by acting on the design of the lip. While the SBLI arises with the increase in V_{cw}, the local fan induced separations arose for all the range of velocities. At 22 and 26kts crosswind speed the two separation characteristics intermittently merge and results in both total pressure and swirl distortion at the AIP. At 30 kts there is a gross unsteady separation which rotates at about 70% of the fan speed and the fan used in these studies exhibits unstable flow behaviour.

Conventional descriptors identified the growth of the distortion at the AIP due to the increase in crosswind speed. The results demonstrate that the distortion is dominated by the circumferential rather than the radial variation of total pressure. The need to account for swirl distortion is also highlighted by both the radial and time variation of swirl intensity. Moreover, the banded spectra and engine order characteristics identified the unsteady signatures of the flow features and the associated total pressure and swirl distortion. Overall, the results highlight the complex unsteady intake-fan aerodynamic interactions as well as the benefits of adopting new approaches for the assessment of unsteady flow distortion to improve the methods beyond the existing conventional distortion descriptors.

1. Contact Author Email Address

mailto: luca.lobuono.030@cranfield.ac.uk

2. Copyright Statement

The authors confirm that they, and/or their company or organization, hold copyright on all of the original material included in this paper. The authors also confirm that they have obtained permission, from the copyright holder of any third party material included in this paper, to publish it as part of

their paper. The authors confirm that they give permission, or have obtained permission from the copyright holder of this paper, for the publication and distribution of this paper as part of the ICAS proceedings or as individual off-prints from the proceedings.

3. Data Availability

All the data supporting the results are included in the article itself, no supplementary source data are required.

4. Acknowledgements

L. Lobuono was supported by the Engineering and Physical Sciences Research Council [grant number EP/W524529/1], Rolls Royce plc., and Cranfield University. R. Christie and D. MacManus were partially funded by Innovate UK FANFARE project (113286).

References

- [1] United Kingdom Department for Transport, "Jet Zero Strategy Delivering net zero aviation by 2050," 2022. Accessed: May 01, 2024. [Online]. Available: https://www.gov.uk/government/publications/jet-zero-strategy-delivering-net-zero-aviation-by-2050
- [2] H. Hoheisel, "Aerodynamic aspects of engine-aircraft integration of transport aircraft," *Aerosp Sci Technol*, vol. 1, no. 7, pp. 475–487, 1997, doi: http://dx.doi.org/10.1016/S1270-9638(97)90009-2.
- [3] A. Peters, Z. S. Spakovszky, W. K. Lord, and B. Rose, "Ultrashort nacelles for low fan pressure ratio propulsors," *J Turbomach*, vol. 137, no. 2, Feb. 2015, doi: 10.1115/1.4028235.
- [4] F. Tejero, M. Robinson, D. G. MacManus, and C. Sheaf, "Multi-objective optimisation of short nacelles for high bypass ratio engines," *Aerosp Sci Technol*, vol. 91, pp. 410–421, Aug. 2019, doi: 10.1016/j.ast.2019.02.014.
- [5] A. N. Rao, P. Sureshkumar, S. Stapelfeldt, B. Lad, K.-B. Lee, and R. P. Rico, "Unsteady Analysis of Aeroengine Intake Distortion Mechanisms: Vortex Dynamics in Crosswind Conditions," *J Eng Gas Turbine Power*, vol. 144, no. 12, Oct. 2022, doi: 10.1115/1.4055279.
- [6] T. Cao, N. R. Vadlamani, P. G. Tucker, A. R. Smith, M. Slaby, and C. T. J. Sheaf, "Fan-Intake interaction under high incidence," *J Eng Gas Turbine Power*, vol. 139, no. 4, 2017, doi: 10.1115/1.4034701.
- [7] A. Yeung, N. R. Vadlamani, T. Hynes, and S. Sarvankar, "Quasi 3D nacelle design to simulate crosswind flows: Merits and challenges," *International Journal of Turbomachinery, Propulsion and Power*, vol. 4, no. 3, Aug. 2019, doi: 10.3390/ijtpp4030025.
- [8] N. R. Vadlamani and P. G. Tucker, "Eddy resolving simulations of intake under crosswinds," in *ERCOFTAC Series*, vol. 25, Springer, 2019, pp. 523–529. doi: 10.1007/978-3-030-04915-7_69.
- [9] W. Zhang and M. Vahdati, "A parametric study of the effects of inlet distortion on fan aerodynamic stability," *J Turbomach*, vol. 141, no. 1, Jan. 2019, doi: 10.1115/1.4041376.
- [10] A. Awes, A. Brosse, G. Dufour, X. Carbonneau, and B. Godard, "Effect of a vortex distortion on the operability of an ultra-high bypass ratio fan," 2020. [Online]. Available: http://asmedigitalcollection.asme.org/GT/proceedings-pdf/GT2020/84065/V02AT32A024/6614145/v02at32a024-gt2020-14596.pdf
- [11] W. Zhang, "Influence of inlet distortion on fan aerodynamic performance," PhD thesis, Imperial College London, 2019.
- [12] J. P. Murphy and D. G. MacManus, "Intake ground vortex prediction methods," *J Aircr*, vol. 48, no. 1, pp. 23–33, 2011, doi: 10.2514/1.46221.
- [13] S. Zantopp, D. MacManus, and J. Murphy, "Computational and experimental study of intake ground vortices," *Aeronautical Journal*, vol. 114, no. 1162, pp. 769–784, 2010, doi: 10.1017/S0001924000004255.
- [14] N. Mishra, D. MacManus, and J. Murphy, "Intake ground vortex characteristics," *Proc Inst Mech Eng G J Aerosp Eng*, vol. 226, no. 11, pp. 1387–1400, Nov. 2012, doi: 10.1177/0954410011424092.
- [15] S. Tambe, U. B. Bartolom', B. Oseguera, and A. G. Rao, "Performance of a low speed axial fan under distortion: an experimental investigation," in *Proceedings of ASME Turbo Expo 2020 Turbomachinery Technical Conference and Exposition GT2020 September 21-25, 2020, Virtual, Online*, 2020. doi: 10.1115/GT2020-14956.
- [16] D. Boldman, C. Iek, D. Hwang, M. Larkin, and P. Schweiger, "Effect of a rotating propeller on the separation angle of attack and distortion in ducted propeller intakes," in *31st Aerospace Sciences Meeting*, in Aerospace Sciences Meetings., American Institute of Aeronautics and Astronautics, 1993. doi: doi:10.2514/6.1993-17.
- [17] M. Carnevale, F. Wang, A. B. Parry, J. S. Green, and L. Di Mare, "Fan similarity model for the fan-intake interaction problem," *J Eng Gas Turbine Power*, vol. 140, no. 5, May 2018, doi: 10.1115/1.4038247.
- [18] M. Carnevale, F. Wang, and L. Di Mare, "Low Frequency Distortion in Civil Aero-engine Intake," *J Eng Gas Turbine Power*, vol. 139, no. 4, Apr. 2017, doi: 10.1115/1.4034600.
- [19] T. Cao, P. Hield, and P. G. Tucker, "Hierarchical immersed boundary method with smeared geometry," *J Propuls Power*, vol. 33, no. 5, pp. 1151–1163, 2017, doi: doi.org/10.2514/1.B36190.
- [20] Y. Ma, J. Cui, N. R. Vadlamani, and P. Tucker, "Effect of Fan on Inlet Distortion: Mixed-Fidelity Approach," *AIAA Journal*, vol. 56, no. 6, pp. 2350–2360, 2018, doi: 10.2514/1.J056858.
- [21] L. Boscagli, D. MacManus, R. Christie, and C. Sheaf, "Effect of Unsteady Fan-Intake Interaction on Short Intake Design," *J Eng Gas Turbine Power*, vol. 146, no. 3, Nov. 2023, doi: 10.1115/1.4063768.
- [22] L. Boscagli, R. Christie, D. MacManus, and T. Piovesan, "Aerodynamics of a short intake in crosswind," *Aerosp Sci Technol*, vol. 129, p. 107826, Aug. 2022, doi: 10.1016/j.ast.2022.107826.
- [23] R. Christie, A. Heidebrecht, and D. MacManus, "An automated approach to nacelle parameterization using intuitive class shape transformation curves," *J Eng Gas Turbine Power*, vol. 139, no. 6, p. 062601, 2017, doi: https://doi.org/10.1115/1.4035283.
- [24] ANSYS Inc., 2021-Ansys ICEM CFD Users Manual. 2021.
- [25] K.-B. Lee, M. Wilson, and M. Vahdati, "Effects of Inlet Disturbances on Fan Stability," *J Eng Gas Turbine Power*, vol. 141, no. 051014, 2018, doi: 10.1115/1.4042204.

- [26] P. Moinier, "Algorithm Developments for an Unstructured Viscous Flow Solver," PhD Thesis, University of Oxford, 1999.
- [27] G. Almendral-Fernandez, D. Amirante, and N. J. Hills, "Use of a zonal hybrid URANS-LES methodology for prediction of rim seal ingestion into a low pressure turbine cavity," in 2018 Joint Propulsion Conference, American Institute of Aeronautics and Astronautics Inc, AIAA, 2018. doi: 10.2514/6.2018-4917
- [28] L. Boscagli, "Aerodynamic Design and Analysis of Aero-engine Short Intakes Under Crosswind Conditions," PhD Thesis, Cranfield University, 2022.
- [29] N. R. Vadlamani, T. Cao, R. Watson, and P. G. Tucker, "Toward future installations: Mutual interactions of short intakes with modern high bypass fans," *J Turbomach*, vol. 141, no. 8, Aug. 2019, doi: 10.1115/1.4044080.
- [30] J. Seddon and E. L. Goldsmith, *Intake aerodynamics*, 2nd edition. Oxford Blackwell Publishing, 1999.
- [31] N. C. Bissinger and T. Breuer, "Basic Principles Gas Turbine Compatibility Intake Aerodynamic Aspects," in *Encyclopedia of Aerospace Engineering*, Wiley, 2010. doi: 10.1002/9780470686652.eae487.
- [32] J. W. Cooley and J. W. Tukey, "An Algorithm for the Machine Calculation of Complex Fourier Series," 1964.
- [33] U. Doll *et al.*, "Non-intrusive flow diagnostics for unsteady inlet flow distortion measurements in novel aircraft architectures," *Progress in Aerospace Sciences*, vol. 130. Elsevier Ltd, Apr. 01, 2022. doi: 10.1016/j.paerosci.2022.100810.
- [34] D. Gil-Prieto, D. G. MacManus, P. K. Zachos, G. Tanguy, and K. R. Menzies, "Convoluted intake distortion measurements using stereo particle image velocimetry," *AIAA Journal*, vol. 55, no. 6, pp. 1878–1892, 2017, doi: 10.2514/1.J055467.
- [35] SAE, "A methodology for assessing inlet swirl distortion," 2017.
- [36] T. Berthelon, A. Dugeai, J. Langridge, and F. Thouverez, "Analysis of Vortex Ingestion Impact on the Dynamic Response of the Fan in Resonance Condition," in *Proceedings of ASME Turbo Expo 2019: Turbomachinery Technical Conference and Exposition GT2019*, Jun. 2019. doi: 10.1115/GT2019-90939.
- [37] M. Vahdati, K.-B. Lee, and P. Sureshkumar, "A Review of Computational Aeroelasticity Of Civil Fan Blades," *International Journal of Gas Turbine, Propulsion and Power Systems*, vol. 11, pp. 22–35, Nov. 2020, doi: 10.38036/jgpp.11.4_22.
- [38] P. Sureshkumar, K.-B. Lee, R. Puente, and S. Stapelfeldt, "Impact of the Spatial Arrangement of Inlet Distortions on Resonant Fan Response," in *Proceedings of Global Power and Propulsion Society, ISSN-Nr: 2504-4400, GPPS Chania22*, Sep. 2022. doi: 10.33737/gpps22-tc-132.